Journal of
Applied Crystallography
ISSN 0021-8898

Received 14 January 2000
Accepted 19 April 2000

X-ray topographic determination of the granular structure in a graphite mosaic crystal: a three-dimensional reconstruction

M. Ohler,[a] M. Sanchez del Rio,[a]* A. Tuffanelli,[b] M. Gambaccini,[b] A. Taibi,[c]† A. Fantini[b] and G. Pareschi[d]

[a]European Synchrotron Radiation Facility, BP 220, F-38043 Grenoble, France, [b]Dipartimento di Fisica, Università di Ferrara and INFN Sezione di Ferrara, Via Paradiso 12, I-44100 Ferrara, Italy, [c]Department of Medical Physics and Bioengineering, University College London, Shropshire House, 11-20 Capper Street, London WC1E 6JA, England, and [d]Osservatorio Astronomico di Brera, Via E. Bianchi 46, I-23807 Merate, Italy. Correspondence e-mail: srio@esrf.fr

Section topographs recorded at different spatial locations and at different rocking angles of a highly oriented pyrolytic graphite (HOPG) crystal allow three-dimensional maps of the local angular-dependent scattering power to be obtained. This is performed with a direct reconstruction from the intensity distribution on such topographs. The maps allow the extraction of information on local structural parameters such as size, form and internal mosaic spread of crystalline domains. This data analysis leads to a new method for the characterization of mosaic crystals. Perspectives and limits of applicability of this method are discussed.

1. Introduction

Highly oriented pyrolytic graphite (HOPG) is an artificial graphite produced by thermal cracking of a hydrocarbon gas and annealing the deposit under pressure. The production process of HOPG and many of its properties and applications have been reviewed by Moore (1973). HOPG samples are used as highly efficient neutron monochromators and for X-ray applications at laboratory and synchrotron radiation sources (Freund, 1998; Ice & Sparks, 1990). HOPG is also an interesting material for optical elements in X-ray mammography (Gambaccini *et al.*, 1995) and for astrophysical devices (Frontera & Pareschi, 1995). HOPG is widely employed because it can be grown to form large mosaic crystals, presents a high X-ray diffraction efficiency, has interesting focusing properties (Ice & Sparks, 1990; Sanchez del Rio *et al.*, 1998) and is readily available in different grades of perfection from commercial companies (*e.g.* Advanced Ceramics, USA, or Optigraph, Russia).

HOPG crystals occur as mosaic crystals with crystallites of microscopic or submicroscopic size. These crystallites are well oriented along the *c* axis of the graphite structure. As a result of the production process of HOPG, the *c* axis is parallel to the surface normal of the crystal. The angular dispersion between crystallites, *i.e.* the 'mosaic spread', of HOPG crystals is typically in the range 0.1–3°. For rotation around the *c* axis, the crystallites display no preferred orientation. As a result of this 'turbostratic structure', only the $00L$ reflections from an HOPG crystal lead to well defined diffraction spots. All other HKL reflections lead to homogeneous Debye–Scherrer diffraction rings. Owing to the structure of graphite, the $00L$ reflections with $L = 1, 3, 5, \ldots$ are forbidden.

Besides these properties, the mosaic spread of the crystallites in HOPG also leads to the particular diffraction characteristics of mosaic crystals. Compared to perfect crystals, they have a lower peak reflectivity but a much higher angular width of the reflection. Both together result in a much higher integrated intensity than that of perfect crystals.

In most models of mosaic crystals, the crystallites are supposed to be perfect crystals with a Gaussian orientation distribution. The mosaicity, which is the full width at half-maximum (FWHM) of this distribution, must be much larger than the Darwin width of the individual perfect crystallites (typically a few arcsec) in order to consider the crystal as a real 'mosaic' crystal. The diffraction of photons in such a mosaic crystal can then be described with a kinematical diffraction theory instead of the dynamical diffraction theory for perfect crystals. Such a description takes into account that photons must penetrate to some depth into the crystal bulk before finding a crystallite correctly oriented and from which they can be diffracted. For the reflection (Bragg) geometry, as in the present case for HOPG, this means that the effective depth in the crystal at which diffraction occurs is much larger than the depths of a few micrometres found in the case of perfect crystals. This effective depth is related to the secondary-extinction length (Zachariasen, 1945).

Several setups can be used to investigate individual crystalline domains in mosaic samples. To study textured materials, Poulsen *et al.* (1997) and Eberl *et al.* (1998) set up an X-ray diffraction experiment with a narrow pencil beam and a

† Permanent address: Dipartimento di Fisica, Università di Ferrara and INFN Sezione di Ferrara, Via Paradiso 12, I-44100 Ferrara, Italy.

receiving slit to define a small gauge volume in the sample. To map the diffraction properties of extended zones in the sample, this 'zero-dimensional' gauge volume is then translated along the three directions through the sample. Such an arrangement was also used by Freund *et al.* (1996) to measure rocking curves of small domains in HOPG.

For a long time, HOPG was considered to be a 'true mosaic crystal' consisting of crystallites with no correlation of their orientation arrangement. However, an arrangement of crystallites to form crystalline domains of similar orientation has been concluded from several experiments. These domains have been visualized by Ohler *et al.* (1997) employed using X-ray diffraction techniques. Ohler *et al.* (1997) employed a narrow and highly collimated beam of monochromatic X-rays to enhance the quality of section topographs. Later, a similar technique was employed to characterize several HOPG samples for X-ray optical applications (Tuffanelli *et al.*, 1999).

Here, further experimental work is described to analyse quantitatively a series of section topographs. The aim of the method is to obtain, for each angular orientation, a three-dimensional mapping of the sample. Therefore, the illuminated zone is scanned through the sample. Thus, angular scans allow the internal mosaic spread of crystalline domains and their mutual orientation distribution to be determined, and translation scans reveal the size and shape of these domains.

The present article explores the possibilities of this new and fast characterization method for the investigation of mosaic crystals. It also introduces a quantitative method to extract the diffraction properties from such sets of topographs.

2. Samples, experimental method and equipment

We have investigated in detail one crystal sample with dimensions of 1.2 × 12.0 × 2.23 mm from the Advanced Ceramics Corporation (formerly Union Carbide Corporation). The same sample was earlier characterized with projection X-ray topography by Ohler *et al.* (1997). In the present investigation, this sample was chosen because it contains large crystalline domains which can be clearly resolved on an X-ray topograph. Note that it has been found (Tuffanelli *et al.*, 1999) that the domain structure of HOPG samples can be very different from that of the sample selected here. These other samples produce very homogeneous X-ray topographs in which the individual crystalline domains cannot be resolved.

X-ray diffraction topography is one of the techniques that is able to reveal defects in crystalline materials with a low defect density. In most cases, a large X-ray beam is employed ('projection topography') and the diffraction image is recorded with a position-sensitive detector, such as an X-ray film or a charge-coupled device (CCD) camera. However, the use of a large X-ray beam is less suited for crystal samples with a high defect density, like HOPG and other mosaic crystals. In such cases, a superposition of images from many individual defects is recorded on the X-ray detector. This renders difficult or even impossible a quantitative analysis of such topographs. This superposition effect can be much reduced with section topography. The reason is that, in contrast to the case of perfect crystals, multiple diffraction events are unlikely in mosaic crystals. Thus, mainly the zone illuminated by the incident beam is imaged on the detector and a diffraction image of a sloping cut through the crystal is recorded (see Fig. 1).

Such experiments were carried out at the BM5 beamline of the European Synchrotron Radiation Facility. This beamline is equipped with a bending magnet of critical energy of 20 keV and a double flat crystal Si(111) monochromator, set to deliver photons of 18 keV for our experiments. The resolving power of this monochromator is $E/\Delta E \simeq 10^4$. A schematic representation of the experimental setup is shown in Fig. 2.

The sample was mounted on a translation stage fixed on the ω circle of a three-axis diffractometer placed at 40 m from the source. The diffraction plane was horizontal. Eventually, aluminium filters of different thickness (1–2 mm) were employed to attenuate the beam in order not to saturate the CCD detector. An entrance slit mounted a few centimetres upstream from the sample defined a beam width of 40 μm in the horizontal plane and of about 3–4 mm in the vertical direction.

An X-ray camera, based on a direct deposition of a gadolinium oxysulfide powder layer onto the CCD surface (Taibi *et*

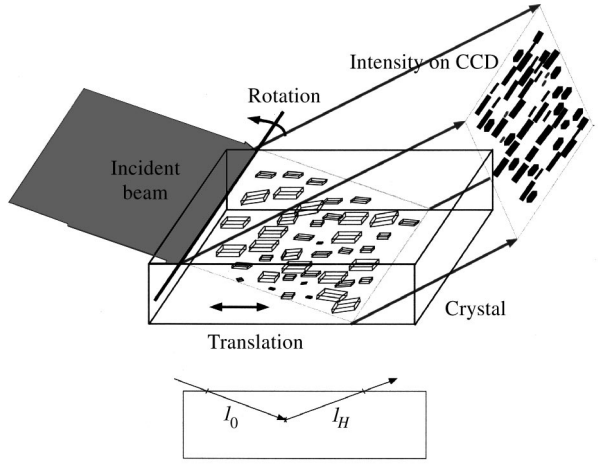

Figure 1
Experimental scheme for recording section topographs from mosaic crystals. The incident beam illuminates a sloping cut through the crystal. In our experiments, the intensity diffracted by such a slice through the crystal is recorded on a CCD. Translation and rotation of the sample allow the diffraction properties of the entire sample at different diffraction angles to be mapped.

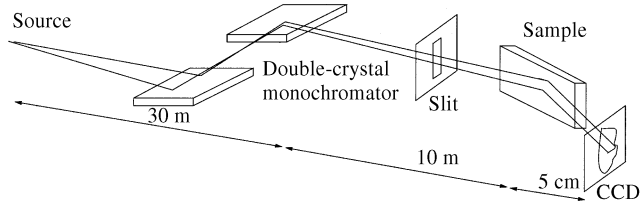

Figure 2
The experimental setup together with the optical system employed at the synchrotron beamline.

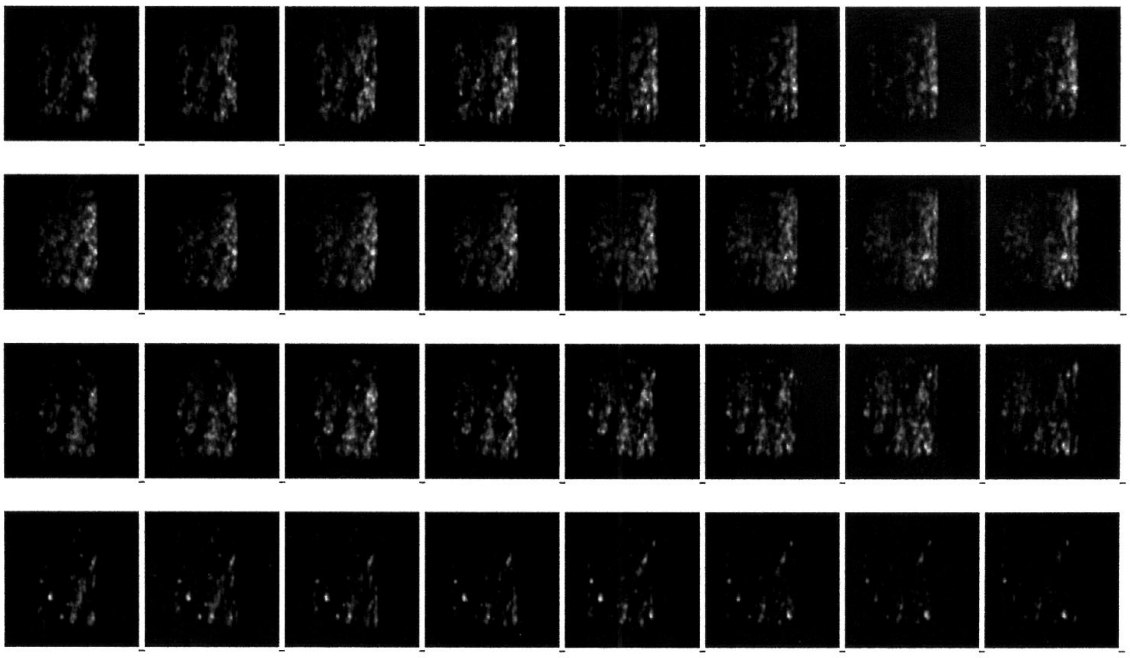

Figure 3
Topographs (raw images) recorded on the 004 reflection for four different rocking angles. The dimension of each topograph is 5 × 5 mm. The horizontal direction is the diffraction plane and the vertical direction corresponds to the basal graphite planes in the sample. The left side of the topograph contains the grains closer to the crystal surface. One can observe how some grains increase their luminosity from one topograph to another, indicating that these particular grains enter the diffraction regime.

al., 1997), was placed about 5 cm downstream from the crystal and perpendicular to the diffracted beam. The pixel pitch of this CCD is 22.5 μm and the 770 × 1152 pixels have a dynamic range of 12 bits. All CCD operations were driven by means of an electronic unit with slow-scan readout and dark-current reduction.

A photodiode detector was also mounted between the sample and the detector. It was used for sample alignment, to measure the incident-beam intensity and to record rocking curves.

The stability of the alignment was demonstrated with identical rocking curves recorded before and after taking the section topographs. In addition, the shapes and widths of rocking curves measured with the photodiode detector are in good agreement with those obtained from the section topographs taken at different angular settings. Therefore, the total intensity on each topograph was calculated by summing the intensity of all pixels.

3. Experimental results

3.1. Rocking curves

Rocking curves were measured at different positions on the sample for the 004 reflection at a Bragg angle of 11.6°. These

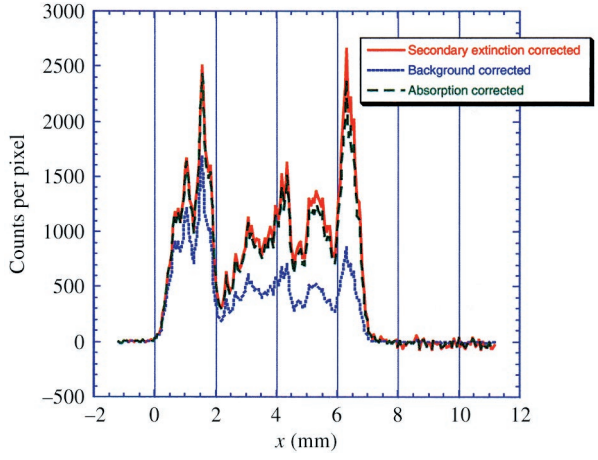

Figure 4
This figure shows the most important steps in the analysis of a section topograph. After a normalization to the synchrotron current and the exposure time, and a background subtraction (labelled 'background corrected'), the images are corrected for absorption (labelled 'absorption corrected'). This step adds the most important correction. Then, the secondary-extinction correction is applied (labelled 'secondary-extinction corrected'), proportional to the local scattering power. The correction added by this step, which is necessary for energy conservation to hold, is hardly visible in the plot and increases with increasing depth in the sample. It corresponds to a maximum correction of 14% of the absorption-corrected intensity.

Table 1
Comparison of the experimental and theoretical values for the absolute peak reflectivity R_{max} and the full width at half-maximum (FWHM) of the rocking curves.

Sample thickness t = 1.2 mm, photon energy E = 18 keV.

004 reflection	Experimental	Zachariasen theory without Compton scattering	Zachariasen theory including Compton scattering
R_{max}	0.22 (5)	0.28	0.24
FWHM (°)	0.26	0.26	0.25

rocking curves may vary slightly from one position on the sample to another and usually are also different for the two faces of a crystal. Table 1 shows the experimental results of one of these scans for the absolute peak reflectivity R_{max} and the FWHM. These values are also compared to simulations using the theory of Zachariasen (1945) implemented in the *XOP* code (Sanchez del Rio & Dejus, 1998). It is well known that the Zachariasen model overestimates the peak reflectivity. For high X-ray energies and low-Z elements, as for the present experiments, Compton scattering may considerably reduce the intensity measured with the detector. Therefore, in our simulations, the absorption coefficient μ accounts for the usual photoelectric term and also for the intensity loss on the topographs caused by Compton scattering ($\mu = \mu_{ph} + \mu_c$). The results of these calculations are also presented in Table 1. It is found that considering the Compton scattering leads to a reasonable agreement between measured and simulated values.

3.2. Section topographs

A total of 81 section topographs were recorded on the 004 reflection at nine different translation steps separated one from the other by 200 µm. This separation is about equal to the projection of the incident-beam width (40 µm) onto the crystal surface. Thus, topographs recorded at different translation positions have no spatial overlap. For each translation position, nine topographs were then taken at different angular settings over the rocking curve. The highest and lowest angles were chosen to correspond to about 10% of the peak reflectivity. A subset of topographs obtained in this way is shown in Fig. 3. These topographs show a granular structure where each spot corresponds to a crystalline domain which is in reflection position. The sizes and shapes of these domains can be determined directly from the topographs.

The adjustment of each new setting and the determination of the required exposure time was performed manually to make sure that the images recorded on the CCD were neither saturated nor underexposed. The exposure times varied from 0.5 to 2.8 s, mainly depending on the angular setting of the rocking curve and on the occasional existence of very luminous spots on the topographs.

4. Reconstruction of local diffraction properties

The analysis of the data collected with the section topographs is performed in two distinct phases. First, the local diffraction-power map is calculated from the topographs. Then, this map is used for a further investigation of the sample.

Firstly, the recorded diffraction topographs are normalized to the exposure time and to the synchrotron current to obtain $I^R(\xi, \eta, t, \theta)$. Here, I^R is the recorded and normalized intensity, ξ and η are coordinates on the topograph, t is the translation and θ is the angular setting of the sample. In this way pixel elements on the CCD can be translated to voxel elements in the sample volume. Shape and size of a voxel element depend on the scattering geometry and on the resolution of the CCD. The aim of the analysis is to extract a diffracting-power map $\sigma(x, y, z, \theta)$, where x, y and z are the spatial coordinates inside the crystal and θ is the rotation angle. The volume reconstruction is performed by converting the ξ, η and t coordinates from the individual topographs to x, y and z coordinates in the crystal. This is performed by geometrical considerations (see below).

To obtain $\sigma(\xi, \eta, t, \theta)$ from $I^R(\xi, \eta, t, \theta)$, at least two effects must be considered: (*a*) absorption and intensity loss caused by scattering in the material and (*b*) the reduction, as a result of the previous scattering events, of the incident beam with increasing depth in the sample ('secondary extinction'). Because each position on a section topograph can be related to a unique beam path in the sample, the correction for absorption and Compton scattering is a simple geometrical problem. Thus, the recorded topographs $I^R(\xi, \eta, t, \theta)$ can be transformed to virtually 'absorption free' and 'Compton scattering free' images, $I^C(\xi, \eta, t, \theta)$.

Now an energy conservation argument can be used for the further evaluation of these new images and secondary extinction can thus be accounted for. At any position l_0 along the incident-beam path, the incident beam is weakened by the previously scattered intensity I^C and thus is

$$I_0(l_0) = I_0(0) - \int_0^{l_0} I^C(l, \theta)\, \mathrm{d}l. \qquad (1)$$

Here $I_0(0)$ is the intensity incident on the surface of the crystal and $I^C(l, \theta)$ is the absorption-corrected and Compton scattering-corrected intensity diffracted at the position l. Here l can be calculated from the ξ and η positions on the topographs. Then, the local diffracting power $\sigma(\xi, \eta, t, \theta)$ is obtained with

$$I^C(\xi, \eta, t, \theta) = \gamma_0 \sigma(\xi, \eta, t, \theta) I_0(l_0), \qquad (2)$$

by solving for $\sigma(\xi, \eta, t, \theta)$. In this equation, γ_0 is the projection of the incident-beam direction on the surface normal of the crystal. When expression (2) is thoroughly derived from the equations underlying the Zachariasen theory, and not as here from energy-conservation arguments, it can be shown that (2) can be used for the analysis of 'absorption corrected' section topographs if the following two conditions are fulfilled: (i) the incident beam must be narrow compared to the resolution voxel in the sample and (ii) multiple scattering events must be very rare.

Fig. 4 shows the results for the most important steps in the calculation of the local scattering power. One line on a topograph along the diffraction plane is chosen. The topograph is first normalized to the synchrotron current and the exposure time and corrected for a linear background. Then, the number of incident photons is calculated from the previously measured reflectivity curve and from the total number of photons on the topograph. Thereafter, the absorption and Compton scattering correction is performed and, finally, the secondary-extinction correction is carried out.

The next step is to build the volume map $\sigma(x, y, z, \theta)$ from the scattering-power topographs $\sigma(\xi, \eta, t, \theta)$. In principle, this

could be performed by building a volume grid in the crystal bulk and histogramming for each volume bin the topograph pixels that will contribute there by following the beam propagation directions. There are, however, some problems with this approach, because the (ξ, η, t) coordinates have different spatial resolution, and because of the high noise introduced by the histogramming process arising from the poor statistics (counts) in each volume bin. Therefore, it is desirable to convert directly the σ values from the topographs into voxel values. For that purpose we can use geometrical considerations, illustrated in Fig. 5: each topograph corresponds to a plane on a sloping cut through the crystal in an adequate reference frame (x, y, z), with the x axis in the direction of the incident beam, y perpendicular to it and lying within the crystal surface, and z perpendicular to both x and y. Then, there is a one-to-one correspondence between each voxel (x, y, z) in this volume and each single pixel (ξ, η) in a topograph for a given value of t.

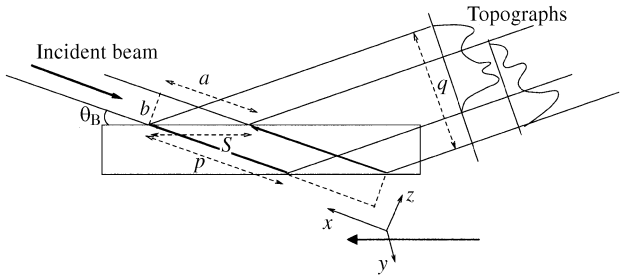

Figure 5
Schematic view of the mosaic crystal and the reference frame (x, y, z) used for volume representation. The distance between the crystal point where the first and the last topographs are recorded is $S = 200\ \mu m \times 8 = 1.6$ mm. The parallelepiped containing the volume has dimensions, in x, of $p + a = (q/\sin\theta_B) + (s/\cos\theta_B) = 24.284 + 1.635 = 25.92$ mm, in y of 22.5 μm × 222 = 5 mm, and in z of $b = S\sin\theta_B = 0.32$ mm.

For our experiments, in the (x, y, z) reference frame (see Fig. 5), the number of voxels of the reconstructed volume is 238 × 222 × 9 for the pixels along x and y and the number of translation positions at which topographs were recorded. The dimensions of each voxel are 109.4 × 22.5 × 41.14 μm. For an optimized visualization of the volume spanned by all voxels, namely for variations along the z direction, we resized by linear interpolation the parallelepiped to 222 × 222 × 55 voxels with new voxel dimensions of 117.8 × 22.5 × 6.74 μm (see the isosurfaces in Fig. 6). This operation is necessary for a correct visualization because of the poor resolution in z (originally only 9 voxels).

Now the volume and angular map $\sigma(x, y, z, \theta)$ of the local scattering power can be used for further analysis. For example, one can investigate the θ profiles and calculate the local peak $R_{max}(x, y, z)$ and integrated reflectivity $S(x, y, z)$ maps. For each position (x, y, z), $R_{max}(x, y, z)$ is the largest $\sigma(x, y, z, \theta)$ for all θ values. The integrated reflectivity $S(x, y, z)$ is approximately proportional to the sum over all θ values of $\sigma(x, y, z, \theta)$. The accuracy of this value can be increased by recording more topographs at different orientations of the sample. These maps give, voxel by voxel, the peak and integrated intensity values of the local rocking curves. Some slices, parallel to the xy planes, of these reconstructed volumes are

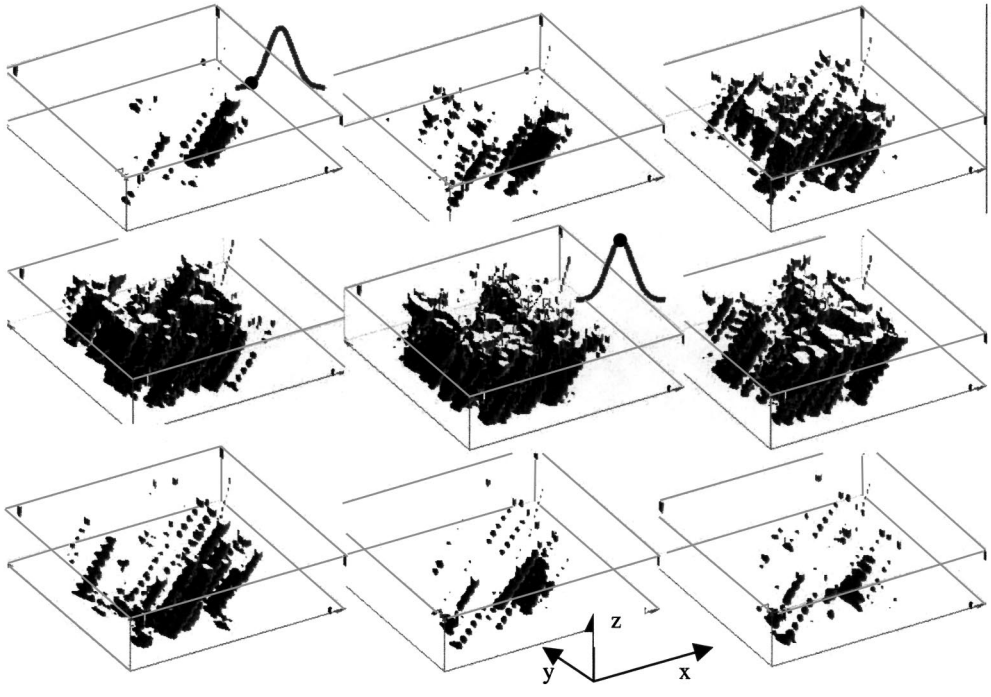

Figure 6
Reconstructed volumes for the nine different rotations. The diffracting power increases and decreases following the rocking-curve rotations. Note that the dimensions of the parallelepiped are 26 mm along x, 5 mm along y and 0.3 mm along z. The reference frame is shown in Fig. 5.

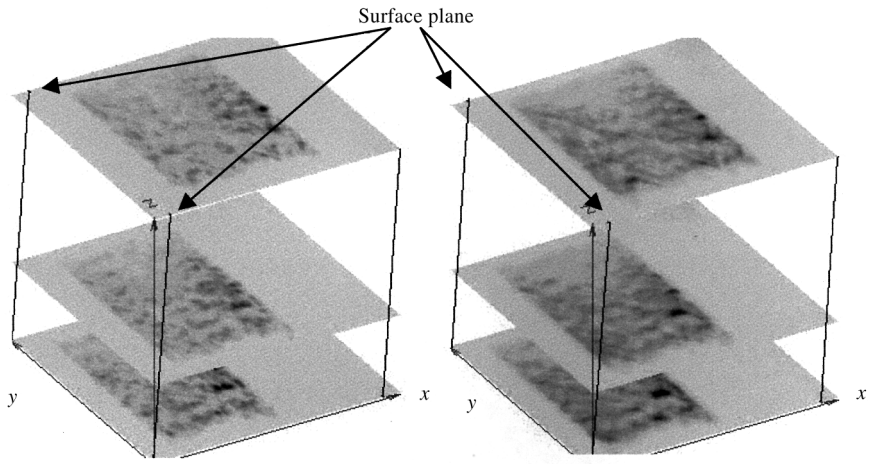

Figure 7
Z slices of the reconstructed peak map $R_{max}(x, y, z)$ (left) and integrated intensity map $S(x, y, z)$ (right). A strong correlation between both reconstructed images can be observed. The reference frame is shown in Fig. 5.

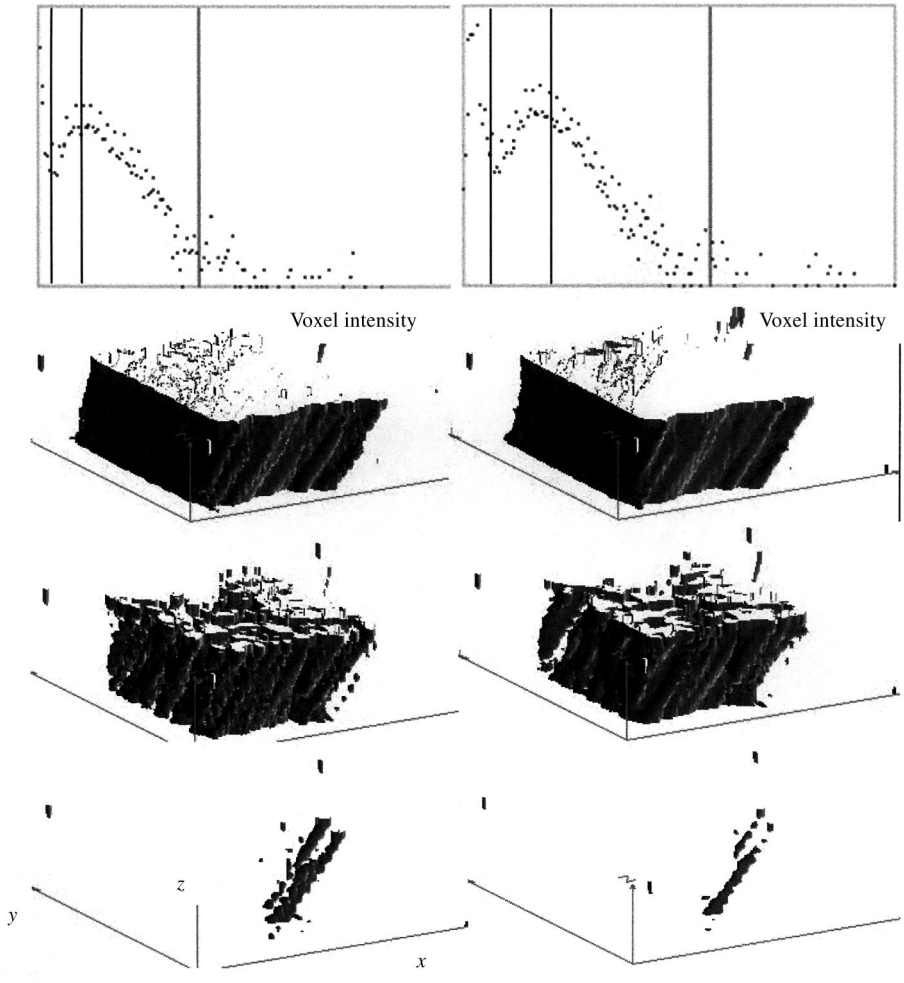

Figure 8
Top: Histograms of the log of the number of occurrences *versus* voxel value for the peak $P(x, y, z)$ (left) and the integrated intensity $S(x, y, z)$ (right) reconstructed maps. The vertical lines indicate the values used for calculating isosurfaces. Bottom: Isosurfaces of the $R_{max}(x, y, z)$ and $S(x, y, z)$ maps corresponding to three different values in the histogram. The upper isosurfaces mainly show the full diffracting volume, the middle ones show the blocks diffracting significantly, and the bottom ones show only the grains that diffract more intensively.

shown in Fig. 7. Isosurfaces of these maps can also be calculated, with different threshold values, as shown in Fig. 8.

Calculating the local FWHM of the diffraction profiles is a more difficult task as data fitting must be performed for each voxel element. For our experiments we have fitted the data to a Gaussian profile to obtain a map $W(\xi, \eta, t)$ of the local FWHM of all $\sigma(\xi, \eta, t, \theta)$. In this procedure, the value for the width was set to zero whenever the fitting routine failed to converge. Fig. 9 shows the results of the fitting operation. An inspection of the results showed that of all voxels in the illuminated volume, about 71% could not be fitted with a Gaussian profile. The other 29% of voxels result in an average FWHM of 0.15° with a standard deviation of 0.02°. Fig. 9 shows the results for the region illuminated by the incident beam at the translation position in the middle of the explored range. The results of this examination were also compared to the results from an on-line inspection of several crystalline domains (as illustrated in Fig. 9). Therefore, regions of interest were defined in the crystal and, for each angular setting, the sum of the intensity from all voxels in this region was calculated. This analysis also resulted in FHWM values close to 0.15°. The high rate of 71% for a failure of the fitting procedure is mainly due to two facts. Firstly, the empty areas surrounding the main square are zones outside the crystal; thus no intensity is found in the topograph and the fit fails. Secondly, the total angular range was not large enough to define a clear peak for some strongly misoriented domains.

5. Summary and perspectives

The main results obtained for the studied sample can be summarized as follows.

(i) The mosaic HOPG crystal studied here is formed by crystalline domains which can be as large as several hundred micrometres along the basal planes. These domains are larger than the spatial resolution achieved in our

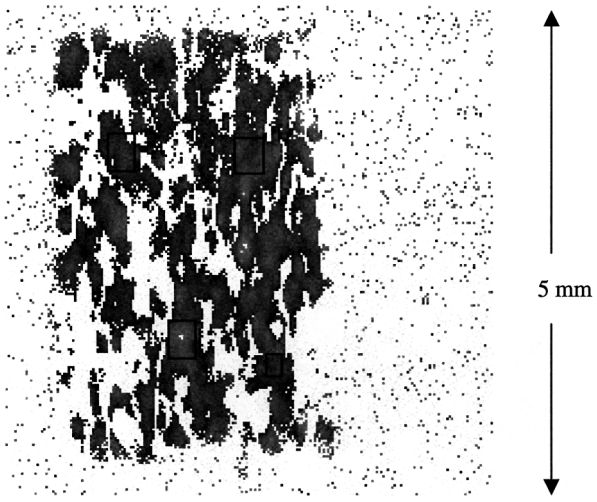

Figure 9
Map of rocking-curve FWHM values $W(\xi, \eta)$ for the middle t value. The averaged FWHM values inside the selected areas are 0.16, 0.14, 0.14 and 0.13° (top left, top right, bottom left, bottom right, respectively). The zero values (white) correspond to points where the fitting routine failed.

experiments. These domains are perfectly visible, both in the maps of reconstructed diffracting power in the volume of the crystal (Fig. 6) and on the raw topographs (Fig. 3) which represent sloping cuts through the volume of the crystal.

(ii) Inside such domains, the crystal structure is still mosaic with a mosaicity of about 0.15°. This is revealed by the calculation of the FWHM of the diffraction power recorded for individual voxels. This internal mosaicity of the domains corresponds to about 60% of the global mosaic spread of the sample obtained by rocking-curve measurements. The measured mosaicity of the domains is a factor of about 400 larger than the diffraction width of a perfect crystal of the same dimensions. Thus, the mosaic behaviour also dominates the diffraction properties of the crystalline domains in the sample. Moreover, the macroscopic mosaic spread between these domains corresponds to about 40% of the mosaic spread of the sample. Similar conclusions have been drawn by Freund *et al.* (1996).

(iii) The reflection widths calculated from individual voxels within a crystalline domain are about equal to the mosaic spread of the entire domain. Thus, within the sensitivity of our measurements, the crystalline domains have no internal structural inhomogeneities.

The capability of the characterization technique proposed here is based on the following aspects. Firstly, it uses standard equipment available at synchrotron radiation sources but needs the low divergence and high intensity available at modern synchrotrons. Secondly, it allows, in a non-destructive way, the visualization of individual domains in mosaic crystals and provides the possibility to measure directly size, internal mosaicity and inter-domain correlations of these domains. With other non-destructive methods, such as high-resolution X-ray diffraction, these parameters have always been deduced from indirect arguments.

The intrinsic limitations of the characterization technique can be summarized as follows. Firstly, the mosaic domains in crystals also lead to a scattering of incident plane waves into a spread of directions within the mean scattering plane and outside this plane (asterism effect). This increases with larger scattering angles and larger mosaic spreads and blurs the recorded diffraction image of the crystal. Secondly, for the study of highly absorbing materials (mosaic crystals other than HOPG), a high dynamic range on the CCD detector system is required. Otherwise, it may be hard to measure grains in the depth of the sample.

Additionally, other limitations are related to the theoretical basis of the reconstruction procedure used here. It must be possible to describe the diffraction properties of the crystal with the Zachariasen model; otherwise the method proposed here cannot be applied. Above all, the mosaic blocks must be located incoherently, which means that there should be no interference effects between them. Furthermore, multiple scattering between domains must be negligible.

Within these limitations, the proposed method can also be applied for the study of other mosaic crystal material. The potential of the method may be further enhanced by the use of a narrower incident beam (which would also allow narrower translation steps), a CCD camera with a higher resolution, a smaller distance between the sample and the camera to reduce image blurring caused by asterism, and, eventually, by developing code that can account for multiple scattering. Therefore, it may be interesting to use also the beams travelling in the forward direction.

We thank A. Souvorov and R. Tucoulou for their assistance during the experiments. A. Freund is acknowledged for fruitful discussions and strong support of this research. MO appreciates discussions with C. Ferrero on the reconstruction algorithm.

References

Eberl, F., Lebrun, J. L. & Cailletaud, G. (1998). *Adv. X-ray Anal.* **42**, CD-ROM. [Proc. Denver X-ray Conf. (1998); http://www.icdd.com.]
Freund, A. K. (1988). *Nucl. Instrum. Methods A*, **266**, 461–466.
Freund, A. K., Munkholm, A. & Brennan, S. (1996). *Proc. SPIE*, **2856**, 69–79.
Frontera, F. & Pareschi, G. (1995). *Exp. Astron.* **6**, 25–31.
Gambaccini, M., Taibi, A., Del Guerra, A., Frontera, F. & Marziani, M. (1995). *Nucl. Instrum. Methods A*, **365**, 248–254.
Ice, G. E. & Sparks, C. J. (1990). *Nucl. Instrum. Methods A*, **291**, 110–116.
Moore, A. W. (1973). *Chemistry and Physics of Carbon*, pp. 11, 69. New York: Marcel Dekker.
Ohler, M., Baruchel, J., Moore, A. W., Galez, Ph. & Freund, A. (1997). *Nucl. Instrum. Methods B*, **129**, 257–260.
Poulsen, H. F., Garbe, S., Lorentzen, T., Juul Jensen, D., Poulsen, F. W., Andersen, N. H., Frello, T., Feidenhans'l, R. & Graafsma, H. (1997). *J. Synchrotron Rad.* **4**, 147–154.
Sanchez del Rio, M. & Dejus, R. J. (1998). *Proc. SPIE*, **3448**, 340–345.

Sanchez del Rio, M., Gambaccini, M., Paresch, G., Taibi, A., Tuffanelli, A. & Freund, A. (1998). *Proc. SPIE*, **3448**, 246–255.
Taibi, A., Del Guerra, A., Gambaccini, M., Marziani, M. & Tuffanelli, A. (1997). *Nucl. Instrum. Methods A*, **392**, 210–213.
Tuffanelli, A., Sanchez del Rio, M., Pareschi, G., Gambaccini, M., Taibi, A., Fantini, A. & Ohler, M. (1999). *Proc. SPIE*, **3773**, 192–198.
Zachariasen, W. H. (1945). *Theory of X-ray Diffraction in Crystals*. New York: Dover.